A phase field model for isothermal crystallization of oxide melts

J. Heulens [*], B. Blanpain, N. Moelans

Department of Metallurgy and Materials Engineering, Katholieke Universiteit Leuven, Kasteelpark Arenberg 44 – Box 2450, B-3001 Heverlee, Belgium

Abstract

We present a multicomponent multi-phase field model for isothermal crystallization of oxide melts. The bulk thermodynamic properties of the liquid as a function of composition are retrieved from the FACT thermodynamic database for oxide systems. For solid phases modeled as stoichiometric in the thermodynamic database, a paraboloid Gibbs energy is introduced with specific constraints to ensure correct phase equilibria and minimal solubility in the stoichiometric phase. The interfacial mobility can show strong anisotropy and the interfacial energy can have weak anisotropy, since both faceted and dendritic growth morphologies are important for crystallization in oxide systems. The possibilities of the model are illustrated with three case studies considering crystallizing and dissolving solid phases in a CaO–Al$_2$O$_3$–SiO$_2$ melt. These case studies show the influence of the diffusion mobilities on the diffusion path, the tie-line selection in a ternary system and the effect of the surface energy on dendritic growth.

1. Introduction

The crystallization of oxide melts is an important phenomenon in many application domains, such as geology [1], pyrometallurgy [2–4], glass ceramics [5] and advanced ceramic materials [6]. The production of glass ceramics, for example, occurs by controlled crystallization of a heavily undercooled liquid to obtain a glassy material with superior mechanical properties [5]. Moreover, production of dense parts of refractory ceramics is often done by liquid-phase sintering, in which the crystallization or dissolution of the powder particles in the interconnected liquid plays an important role [6].

Crystallizing phases often exhibit complex morphologies on the mesoscale, dendrites being a well-known example [7]. The phase field concept has proved to be a very powerful tool [8] for modeling crystallizing microstructures, because it can treat arbitrarily complex interface shapes with minimal mathematical complexity. Kobayashi was the first to successfully simulate a growing dendrite in a pure undercooled metallic liquid using a phase field model [9]. Later, Warren and Boettinger simulated an isothermal constitutional dendrite in a binary alloy [10]. The extension from two phase systems (single dendrite) to multi-phase systems was done by Steinbach et al. [11], introducing the multi-phase approach. Tiaden et al. have developed a framework for coupling diffusion equations to phase field equations [12] in multi-component systems.

The phase field method is mostly applied for metallic systems and the current methodologies do not completely extend to oxide systems. For oxide systems, the composition dependence of thermodynamic functions and diffusion data are typically expressed as a function of oxide components (e.g. CaO, SiO$_2$, ...), whereas for metals, the composition dependence is generally expressed as a function of the elements (e.g. Cu, Fe, ...). The thermodynamic databases for oxides are also based on different models than those for metals. Oxide melts are often modeled using a Modified Quasi-Chemical Model [13] and solid oxide

---

* Corresponding author.

E-mail addresses: jeroen.heulens@mtm.kuleuven.be (J. Heulens), bart.blanpain@mtm.kuleuven.be (B. Blanpain), nele.moelans@mtm.kuleuven.be (N. Moelans).

phases are frequently considered as stoichiometric, which is not compatible with the diffusion equations and diffuse interface approach within a standard phase field model. Furthermore, both dendritic and faceted growth morphologies are important for oxide systems and are frequently observed simultaneously in multi-component oxides.

In this work, we develop a phase field model for isothermal crystallization of oxide systems and work out a coupling with the FACT thermodynamic databases for oxide systems. The model is constructed using a phase field model for multi-phase systems, based on the grain growth model of Moelans et al. [14] and the multi-component approach of Tiaden et al. [12] or Kim et al. [15]. The formulation of the model is given in Section 2 and the link with thermodynamic databases for oxide systems is explained in Section 3. Next, the numerical implementation and simulation parameters are described in Section 4. The capabilities of the model are illustrated and discussed for three case studies in Section 5. Finally, in Section 6, we briefly summarize the results.

2. Model description

2.1. Multiphase approach

In a phase field model for microstructure evolution, the equations are defined and solved over the whole system without prior knowledge about the position of the interfaces. Microstructure evolution in an isothermal system at constant pressure is driven by minimization of the total Gibbs energy. The microstructure of the system is described by a set of continuous non-conserved phase field variables, $\eta_i(\vec{r}, t)$, which are related to the local phase fractions. The total energy, F [J], of a heterogeneous isothermal system with p phases and c components is formulated as a functional of the non-conserved phase field variables, $\eta_i(\vec{r}, t)$, and the conserved concentration variables, $x_k(\vec{r}, t)$:

$$F = \int_V \left(m f_0 + \frac{\kappa}{2} \sum_{i=1}^{p} |\nabla \eta_i|^2 + \sum_{i=1}^{p} \phi_i f^i \right) dV \quad (1)$$

The first term is called the homogeneous free energy, f_0, and is given by:

$$f_0 = \sum_{i=1}^{p} \left(\frac{\eta_i^4}{4} - \frac{\eta_i^2}{2} \right) + \gamma \sum_{i=1}^{p} \sum_{j>i}^{p} \eta_i^2 \eta_j^2 + \frac{1}{4} \quad (2)$$

This function has minima at $(\eta_1, \ldots, \eta_i, \ldots, \eta_p) = (0, \ldots, 1, \ldots, 0)$, which implies a phase field variable equal to 1 where the respective phase is physically present and 0 elsewhere in the system. The second term is the gradient free energy term, which is responsible for the diffuse character of the interfaces where the phase field variables of adjacent phases vary smoothly from 0 to 1 and vice versa. The third term is the contribution of the Gibbs energies of the phases, f^i (J m^{-3}), to the total system energy where the phase fraction ϕ_i is defined as:

$$\phi_i = \frac{\eta_i^2}{\sum_{j=1}^{p} \eta_j^2} \quad (3)$$

Note that these phase fractions, ϕ_i, sum up to 1 by definition, whereas the phase variables, η_i, do not [16]. This is in contrast with the multi-phase field model of Steinbach et al. [11], where the phase field variables, ϕ_i, represent the phase fractions and, therefore, they are subject to an extra constraint, $\sum_{i=1}^{p} \phi_i = 1$. The evolution equation for each phase field variable η_i follows a time-dependent Ginzburg–Landau equation for non-conserved phase fields:

$$\frac{\partial \eta_i}{\partial t} = -L \frac{\delta F}{\delta \eta_i} \quad (4)$$

The model parameters κ, m and L in the equations above are calculated using the following expression:

$$\kappa = \frac{\sum_{i=1}^{p} \sum_{j>i}^{p} \kappa_{i,j} \eta_i^2 \eta_j^2}{\sum_{i=1}^{p} \sum_{j>i}^{p} \eta_i^2 \eta_j^2} \quad (5)$$

for κ and analogous expressions for m and L. The parameters $m_{i,j}$, $\kappa_{i,j}$, γ and $L_{i,j}$ relate to the interface width, energy and mobility [14]. At an interface between two phases i and j, only η_i and η_j differ from 0, hence $\kappa = \kappa_{i,j}$ at the interface between phases i and j. At triple and multi-junctions, the values for κ, m and L interpolate between their values of the adjacent phases. In the presented model, $\gamma = 1.5$, and therefore the surface energy $\sigma_{i,j}$ (J m^{-2}) and width $l_{i,j}$ (m) of a certain interface ij can be calculated analytically [14]:

$$\sigma_{i,j} = \frac{\sqrt{2}}{3} \sqrt{m_{i,j} \kappa_{i,j}} \quad (6)$$

$$l_{i,j} = \sqrt{\frac{8 \kappa_{i,j}}{m_{i,j}}} \quad (7)$$

2.2. Multicomponent approach

Eiken et al. [17] introduced a framework for the chemical thermodynamics in a phase field model for multi-component systems in which the diffuse interface is assumed to be a mixture of the adjacent phases, each with its own phase composition. The phase concentrations x_k^i of component k in phase i differ from the local concentrations x_k in the interface region. They are unambiguously defined at each point of the system by the requirement of locally equal diffusion potentials and a mass balance, at constant molar volume, for that component:

$$\tilde{\mu}_k^1 = \cdots = \tilde{\mu}_k^i = \cdots = \tilde{\mu}_k^p \quad (8)$$

$$x_k = \sum_{i=1}^{p} \phi_i x_k^i \quad (9)$$

The Gibbs energies of the different phases, f^i in Eq. (1), are evaluated for the phase concentrations x_k^i.

In many aspects, it is more suitable to use oxides as components (CaO, SiO$_2$, ...) in a phase field model for oxide systems. First, oxides are often chosen as the independent components in the thermodynamic models for oxide systems, such as the Modified Quasi-Chemical Model [13,18]. Secondly, experimental diffusion data are fre-

quently reported in the oxides [19]. Thirdly, choosing oxide components allows for distinguishing between different valencies (e.g. FeO and Fe_2O_3). In a system with c components, $c-1$ independent components and one reference component are chosen. In this phase field model for silicate systems, SiO_2 is chosen as the reference component. The diffusion potentials $\tilde{\mu}_k^i$ of these independent components are defined as the first derivative of the Gibbs energy f^i or, analogously, as the difference between the chemical potential of component k and SiO_2 [17]:

$$\tilde{\mu}_k^i = \frac{\partial f^i}{\partial x_k^i} = \mu_k^i - \mu_{SiO_2}^i \tag{10}$$

For each component k, Eqs. (8) and (9) form a system of p equations and p variables, namely the phase concentrations of component k.

2.3. Phase field equations

The functional derivative on the right-hand side of Eq. (4) is calculated according to the Euler–Lagrange theorem for a functional of the form $F = \int_V f(\vec{r}, \eta_i, \nabla \eta_i)$:

$$\frac{\partial \eta_i}{\partial t} = -L \frac{\delta F}{\delta \eta_i} = -L \left(\frac{\partial f}{\partial \eta_i} - \nabla \cdot \frac{\partial f}{\partial \nabla \eta_i} \right) \tag{11}$$

$$\frac{\partial f}{\partial \eta_i} = m \frac{\partial f_0}{\partial \eta_i} + \frac{\partial}{\partial \eta_i} \left(\sum_{j=1}^p \phi_j f^j \right) \tag{12}$$

$$\frac{\partial f_0}{\partial \eta_i} = \eta_i^3 - \eta_i + 2\gamma \eta_i \left(\sum_{j \neq i}^p \eta_j^2 \right) \tag{13}$$

$$\frac{\partial}{\partial \eta_i} \left(\sum_{j=1}^p \phi_j f^j \right) = \sum_{j=1}^p \left[\left(f^j - \sum_{k=1}^{c-1} \tilde{\mu}_k x_k^j \right) \frac{\partial \phi_j}{\partial \eta_i} \right] \tag{14}$$

The last equation is derived using the equality of diffusion potentials (8) and the mass balance (9) for all components [16]. Many minerals exhibit a faceted form when growing in a melt [1] at low supersaturations. At high supersaturation, the mineral can grow in dendrite form. Since, for oxide systems, faceted growth is generally dictated by a strong anisotropy in interface kinetics, faceted growth is modeled in the phase field model using a strong anisotropy in the kinetic coefficient, L, which is related to the interface mobility:

$$L_{i,j} = \overline{L_{i,j}} \psi_{i,j} \left(\theta_{i,j} - \theta_{i,j}^0 \right) \tag{15}$$

with $\theta_{i,j}$ the orientation of the interface:

$$\theta_{i,j} = \arctan \left| \frac{\nabla_y \eta_i - \nabla_y \eta_j}{\nabla_x \eta_i - \nabla_x \eta_j} \right| \tag{16}$$

The function $\psi_{i,j}$ must have sharp cusps at the facet plane orientations. A possible function to incorporate such cusps is [20]:

$$\psi_{i,j}(\theta) = 1 - \beta_{i,j} + 2\beta_{i,j} \tanh \left(\frac{r_{i,j}}{\left| \tan \left(\frac{a_{i,j}}{2} \theta \right) \right|} \right) \tag{17}$$

Here, $\beta_{i,j}$ is a measure for the *depth* of the cusps and hence the mobility difference between the fast and slow crystal planes. On the other hand, $r_{i,j}$ is a measure of the *sharpness* of the cusps and controls therefore the corner formation at the edges of two crystal planes. $a_{i,j}$ is the mode of anisotropy and mostly 4 or 6 for common minerals like spinel or corundum. In the case of dendrite growth, the mineral grows diffusion controlled and the morphology is determined by weak anisotropy in the interface energy. The orientation dependent interface energy $\sigma_{i,j}$ induces orientation dependent $m_{i,j}$ and $\kappa_{i,j}$ parameters for each interface. Both parameters have the same orientation-dependent function $\lambda_{i,j}(\theta_{i,j})$:

$$\kappa_{i,j} = \overline{\kappa_{i,j}} \lambda_{i,j}(\theta_{i,j}) \tag{18}$$
$$m_{i,j} = \overline{m_{i,j}} \lambda_{i,j}(\theta_{i,j}) \tag{19}$$

The function $\lambda_{i,j}(\theta_{i,j})$ describes the anisotropy of the interfacial energy, and for weak anisotropy is taken as follows [9]:

$$\lambda_{i,j}(\theta_{i,j}) = 1 + \delta_{i,j} \cos(a_{i,j}\theta_{i,j}) \tag{20}$$

where $a_{i,j}$ is the mode of the anisotropy and $\delta_{i,j} < 1/(a_{i,j}^2 - 1)$ is the amplitude of the anisotropy. The variational derivation of the phase field equations is more complicated due to its dependence on $\nabla \eta_i$. However, the model remains rotation invariant [21].

In the current model, every interface can have arbitrary properties and strong anisotropy in the interface mobility or weak anisotropy in the interfacial energy. Fig. 1 shows a simulation with three phase fields where two phases grow simultaneously from a melt but with different growth kinetics.

2.4. Diffusion equations

The diffusion equation for each of the $c-1$ independent components is given by [17]:

$$\frac{\partial x_k}{\partial t} = \nabla \cdot \left[\sum_{i=1}^p \phi_i \left(\sum_{l=1}^{c-1} M_{kl}^i \nabla \tilde{\mu}_l^i \right) \right] \tag{21}$$

The elements M_{kl}^i form a mobility matrix $\boldsymbol{M}^i$ for phase i, which relates to the interdiffusion matrix $\boldsymbol{D}^i$ and thermodynamic factors matrix $\boldsymbol{G}^i$ according to the following formula [17]:

$$\boldsymbol{D}^i = \boldsymbol{M}^i \boldsymbol{G}^i \qquad G_{r,s}^i = \frac{\partial \tilde{\mu}_r^i}{\partial x_s^i} = \frac{\partial^2 f^i}{\partial x_r^i \partial x_s^i} \tag{22}$$

In oxide melts, the cross-diffusion or uphill diffusion effects can be substantial [22]. It is therefore important to incorporate the full mobility matrix of each solution phase in the model. The diffusion equations are expressed in mole fraction of the oxide components, which is justified since the diffusion is assumed to be substitutional in terms of the oxide components.
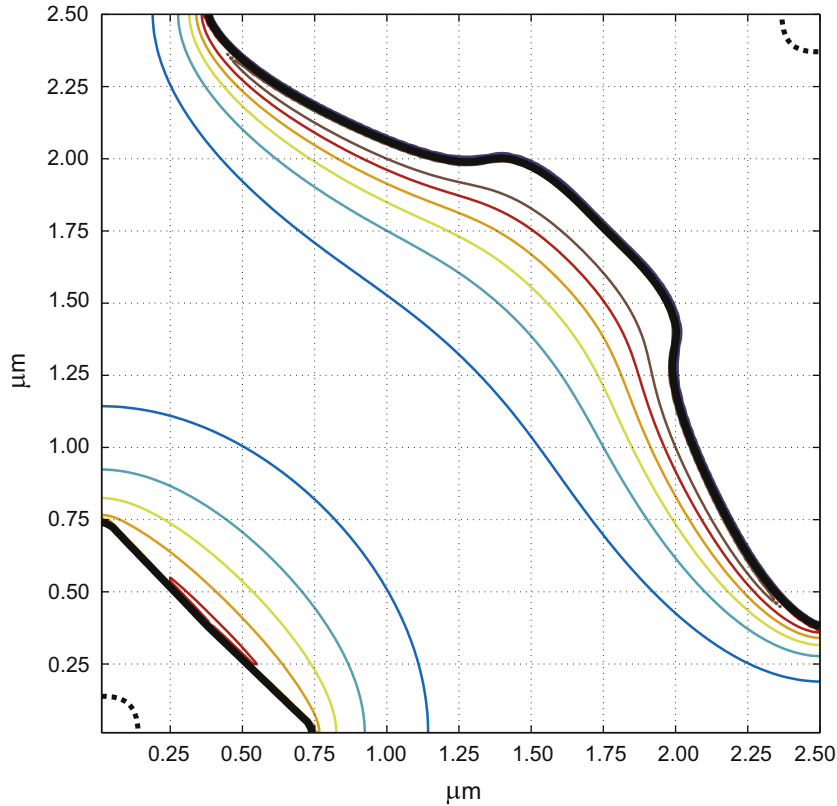
Fig. 1. An example simulation for a binary model system to show the effect of different interface kinetics on the growth form of a crystal. The lower left interface has a strongly anisotropic mobility while the upper right interface has an isotropic mobility but weak anisotropy in the interfacial energy. Both anisotropy symmetries are fourfold. The interfaces are marked in bold lines and the colored thin lines indicate the contour lines of the diffusion field. The dotted line indicates the position of the initial nucleus. (For interpretation of the references to color in this figure legend, the reader is referred to the web version of this article.)

3. Coupling with thermodynamic database

It gives a substantial numerical advantage to approximate the Gibbs energies of the different phases, f^i, in Eqs. (8) and (9) by a second-order Taylor approximation, $\hat{f}^i$, around $\hat{x}^i = (\hat{x}_1^i, \ldots, \hat{x}_k^i, \ldots, \hat{x}_{c-1}^i)$:

$$\hat{f}^i = \sum_{k=1}^{c-1} \left(\frac{A_{kk}^i}{2} \left(x_k^i - \hat{x}_k^i \right)^2 \right)$$
$$+ \sum_{k=1}^{c-1} \left(\sum_{l>k}^{c-1} \left(A_{kl}^i (x_k^i - \hat{x}_k^i)(x_l^i - \hat{x}_l^i) \right) \right)$$
$$+ \sum_{k=1}^{c-1} \left(B_k^i (x_k^i - \hat{x}_k^i) \right) + C^i \tag{23}$$

The parameters arrays A, B and C are retrieved at every concentration $\hat{x}^i$ from a thermodynamic database as:

$$A_{kl}^i = \left. \frac{\partial^2 f^i}{\partial x_k^i \partial x_l^i} \right|_{\hat{x}^i} \qquad B_k^i = \left. \frac{\partial f^i}{\partial x_k^i} \right|_{\hat{x}^i} \qquad C^i = f^i |_{\hat{x}^i} \tag{24}$$

Fig. 2 shows, for three concentrations $\hat{x}^i = \{\bar{x}_1, x_{eq}^L, \bar{x}_2\}$, the second-order approximation of the Gibbs energy of the liquid phase. Eqs. (8) and (9) now result in a linear system of equations where A, B and C are calculated at the local

phase composition and the system of equations is solved for the new phase composition. The phase field model is linked with the FToxid database for oxide systems from the FACTSage package [23]. Therefore, the composition domain is discretized on a square grid ($\Delta x = 0.001$) and A, B and C are calculated at every grid point using ChemApp [24]. Since ChemApp contains no built-in routine to calculate the second derivative of the Gibbs energy of a phase, a centered finite difference scheme,

$$\frac{\partial^2 f^i}{\partial x_k^i \partial x_l^i} = \frac{\partial \tilde{\mu}_k^i}{\partial x_l^i} = \frac{\tilde{\mu}_k^i(x_l^i + \delta x) - \tilde{\mu}_k^i(x_l^i - \delta x)}{2\delta x} \tag{25}$$

was implemented to determine these derivatives. It seems that $\delta x = 10^{-6}$ is a good choice for the finite difference in the equation above. At large δx, the discretization is too coarse to yield reliable values for the derivatives, while for decreasing δx the accuracy of the ChemApp routines decreases. The calculated molar Gibbs energies and diffusion potentials are divided by a constant molar volume to obtain volumetric quantities. The Gibbs energy in Eq. (14) and diffusion potentials in Eqs. (14) and (21) are calculated at the local phase concentrations using bilinear interpolation between the tabulated values of respectively C and B (see Eq. (24)). The second-order approximation of the
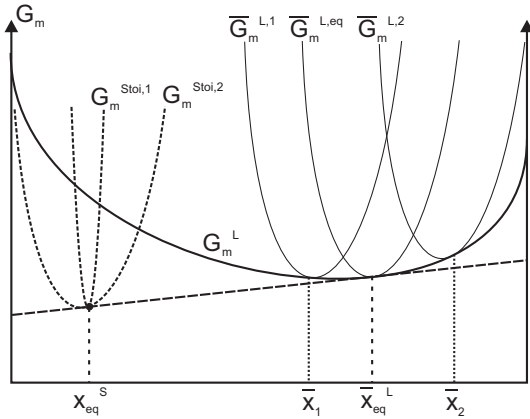
Fig. 2. Binary representation of the paraboloid construction for the Gibbs energy of a stoichiometric phase. This figure shows the molar Gibbs energies of a stoichiometric solid phase ($G_m^{Stoi,1}$ or $G_m^{Stoi,2}$) and a liquid phase (G_m^L). The paraboloid for the stoichiometric phase is constructed to ensure the correct Gibbs energy value at the stoichiometric composition and an equal chemical potential for all components between both phases. The introduced solubility in the stoichiometric phase depends on the curvature of the paraboloid. For illustration, a parabola with high ($G_m^{Stoi,1}$) and low ($G_m^{Stoi,2}$) curvature is plotted for the stoichiometric phase. The three parabolas shown as solid thin lines ($\overline{G}_m^{L,1}, \overline{G}_m^{L,eq}, \overline{G}_m^{L,2}$) represent second-order approximations of the Gibbs energy of the liquid, used to solve Eqs. (8) and (9), at three different compositions ($\bar{x}_1, \bar{x}_{eq}, \bar{x}_2$). Note that the equilibrium composition in the solid phase, x_{eq}^S, does not coincide with the minimum of the solid phase parabola.

Gibbs energies in Eq. (23) is only used to solve the system of Eqs. (8) and (9).

The solid phases in oxide systems are often modeled as purely stoichiometric compounds in thermodynamic databases, which is incompatible with a continuum model formulation and does not allow for diffusion through this phase. Therefore, a paraboloid Gibbs energy is constructed for stoichiometric phases, inspired by the technique proposed in [25], that ensures the correct Gibbs energy value at the stoichiometric composition and for all components the same chemical potentials as in the solution phase at a given initial composition, as shown in Fig. 2. This requirement determines the values of **B** and **C**. Furthermore, the curvature of the paraboloid, **A**, has to be sufficiently high to minimize the solubility in the stoichiometric phase and the deviation from the expected equilibrium compositions in the coexisting solution phases (see Section 5.2). The curvature is also limited because the linear system to solve the phase concentrations becomes ill-conditioned for high curvatures. Stoichiometric phases can thus be treated in a similar way as the solution phases in Eqs. (8) and (9), with **A**, **B**, **C** constant for all phase concentrations.

4. Numerical implementation and simulation setup

4.1. Numerical implementation

The phase field and diffusion equations, (11) and (21), are discretized on an equidistant numerical grid using finite differences in the FORTRAN programming language. Central finite differences are used in space and forward differences in time. A nine-point stencil is used to calculate the spatial gradients to reproduce the anisotropic behavior of the interfaces with higher accuracy. The gradient in one direction at a certain grid point is weighted with the gradients with the adjacent grid points in the other direction, using the weighing factors $\frac{1}{8}, \frac{6}{8}, \frac{1}{8}$. The numerical calculation of the gradient in x-direction of an arbitrary variable ζ at grid point (x, y) is given:

$$\nabla_x \zeta = \frac{1}{8} \frac{\zeta(x+1, y-1) - \zeta(x, y-1)}{\Delta x} + \frac{6}{8}$$
$$\times \frac{\zeta(x+1, y) - \zeta(x, y)}{\Delta x} + \frac{1}{8}$$
$$\times \frac{\zeta(x+1, y+1) - \zeta(x, y+1)}{\Delta x} \quad (26)$$

The boundary conditions (Neumann or periodic) are implemented using ghost nodes at the border of the numerical domain. The program sequence for every time step is as follows:

1. updating the values of η_i and x_k on the ghost nodes according to the boundary conditions,
2. calculating ϕ_i (Eq. (3)) and x_k^i (by solving a linear system of Eqs. (8) and (9)),
3. calculating κ, L and m (Eq. (5)),
4. calculating new phase field values, η_i (Eq. (11)),
5. calculating new component concentrations, x_k (Eq. (21)).

The linear system of Eqs. (8) and (9), to calculate the phase concentrations, is numerically solved using the ludcmp and lubksb subroutines from Ref. [26]. There must be at least 8 grid points in the diffuse interface to resolve the phase field profiles well. The program code is parallelized and executed on a high performance computer cluster [27] using 100 processors for the two-dimensional (2-D) simulations shown in Fig. 8. The phase field equations are only solved in the proximity of interfaces to increase the numerical efficiency, while the diffusion equations are solved everywhere.

4.2. Simulation setup

The presented model is employed for two 1-D and one 2-D simulations of a solid phase growing or dissolving in a CaO–Al$_2$O$_3$–SiO$_2$ melt, for which an isothermal section at 1350 °C is given in Fig. 3. In the simulation, there are two phases present ($\eta_1 =$ liquid, $\eta_2 =$ solid) and 1 interface (12 = solid–liquid). The interface width for both cases is chosen in the thin interface limit [28], which gives $l_{12} = 10^{-7}$ m. Choosing eight grid points in the diffuse interface yields a spatial discretization of 0.125×10^{-7} m. The time step is restricted by the diffusion equations and is taken at $\Delta t = 3.5 \times 10^{-9}$ s for 1-D systems and $\Delta t = 2.0 \times 10^{-9}$ s for 2-D systems. A value of $\sigma_{12} = 0.3$ J m^{-2}
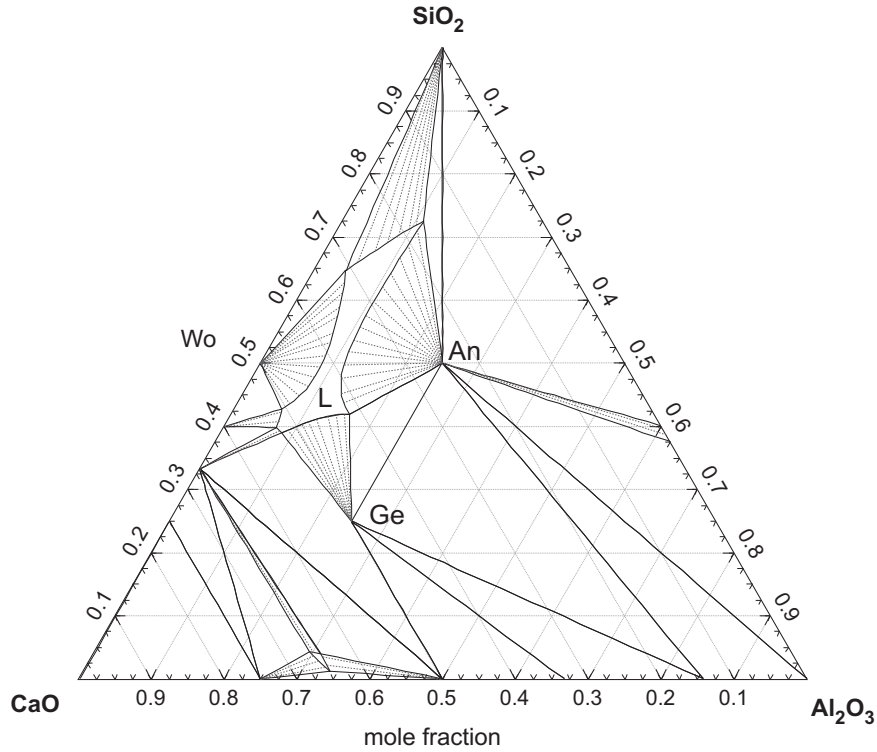
Fig. 3. Isothermal section of the CaO–Al$_2$O$_3$–SiO$_2$ system at 1350 °C (calculated with FACTSage [23]). All simulations are done in the triangle wollastonite (Wo)–gehlenite (Ge)–anorthite (An). The compositions are in mole fractions.

is chosen, which implies $\kappa_{12} = 0.225 \times 10^{-7}$ J m^{-3} and $m_{12} = 1.8 \times 10^7$ J m^{-1}. The anisotropy in interface mobility and energy is set to 0 in 1-D simulations and A of the stoichiometric solid phase is taken to be 10 times larger than that of the liquid phase at its initial composition. The phase field mobility, L_{12}, is chosen to ensure diffusion controlled growth (or dissolution) of the mineral (as explained in Ref. [16]). Therefore $L_{12} = 0.01$ for the growth of wollastonite (see Section 5.3) and $L_{12} = 0.0005$ for the dissolution of gehlenite (see Section 5.1). The molar volume of all components in all phases is taken to be constant and is calculated from Ref. [29]. An average value of $V_m = 23.6 \times 10^{-6}$ m^3 mol^{-1} is obtained for the composition range of the performed simulations. For the crystallizing wollastonite, the mobility matrix of the liquid is calculated using Eq. (22). The interdiffusion matrix $\boldsymbol{D}^L$ is calculated at $T = 1350$ °C using Ref. [30] and the thermodynamic factors matrix $\boldsymbol{G}^L$ is calculated at the initial liquid composition using ChemApp:

$$\boldsymbol{D}^L = \begin{bmatrix} 8.734 & -2.464 \\ -3.948 & 5.977 \end{bmatrix} \times 10^{-11} \quad [\text{m s}^{-2}] \quad (27)$$

$$\boldsymbol{G}^L = \begin{bmatrix} 1.375 & 1.420 \\ 1.420 & 4.307 \end{bmatrix} \times 10^{10} \quad [\text{J m}^{-3}] \quad (28)$$

$$\boldsymbol{M}^L = \boldsymbol{D}^L(\boldsymbol{G}^L)^{-1} = \begin{bmatrix} 0.1053 & -0.0405 \\ -0.0653 & 0.0354 \end{bmatrix} \times 10^{-19} \quad (29)$$

For the dissolving gehlenite, the diffusion matrix is of the same order of magnitude but the diagonal elements are altered to investigate their effect on the tie-line selection (see

Fig. 4). The mobility matrix $\boldsymbol{M}^S$ in the solid phase does not affect steady-state growth and is taken to be of the same order of magnitude as $\boldsymbol{M}^L$ in the liquid phase to avoid solute trapping effects [31], and off-diagonal elements equal to 0.

5. Simulation results and discussion

5.1. Gehlenite dissolving in a CaO–Al$_2$O$_3$–SiO$_2$ melt

A first simulation is done where gehlenite is brought into contact with a liquid, which has a composition outside the two-phase region, at 1400°. At the initial condition, half of the simulation domain is gehlenite at its stoichiometric composition ($x^0_{\text{CaO}} = 0.5, x^0_{\text{Al}_2\text{O}_3} = 0.25$) while the other half is liquid with a composition of ($x^0_{\text{CaO}} = 0.45, x^0_{\text{Al}_2\text{O}_3} = 0.10$). The resulting diffusion profiles are plotted in Fig. 4 for three different ratios of diffusion mobilities. These diffusion profiles clearly show the influence of the diffusion kinetics in the liquid on the local equilibrium or tie-line at the solid–liquid interface. The off-diagonal elements in the mobility matrix of the liquid are 0, so all cross-diffusion effects are caused by the concentration-dependent chemical potentials of both independent components.

5.2. Validation of the paraboloid Gibbs energies for stoichiometric phases

As explained in Section 3, a paraboloid Gibbs energy is constructed for stoichiometric phases, such as gehlenite. For a stoichiometric phase, $\boldsymbol{A}$, $\boldsymbol{B}$ and $\boldsymbol{C}$ are constant over
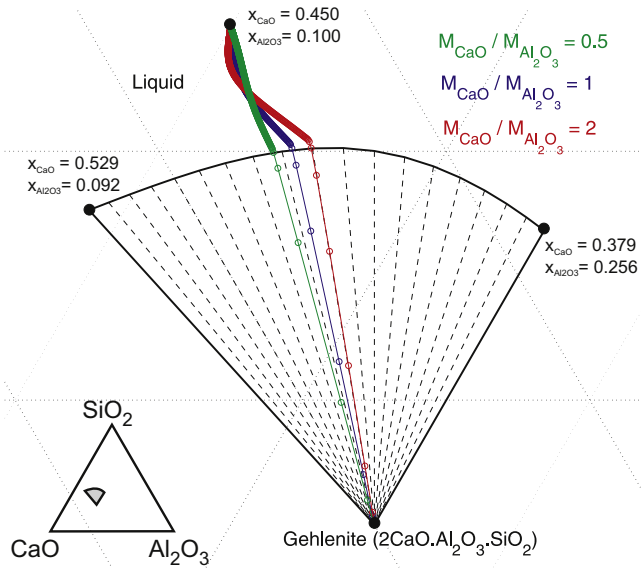
Fig. 4. Magnification of the isothermal section at 1400 °C at the two-phase gehlenite-liquid region. The simulation result of dissolving gehlenite is plotted on this section. The inset at the bottom left indicates the position of the two-phase region, considered in the simulation, in the ternary phase diagram. The composition of the outer points of this region are given as well. The figure shows how the ratio of diffusion mobilities in the liquid phase influences the selection of the tie-line in the two-phase region. Note that the off-diagonal elements are 0 and all cross-diffusion effects are caused by the concentration-dependent chemical potentials of both independent components.
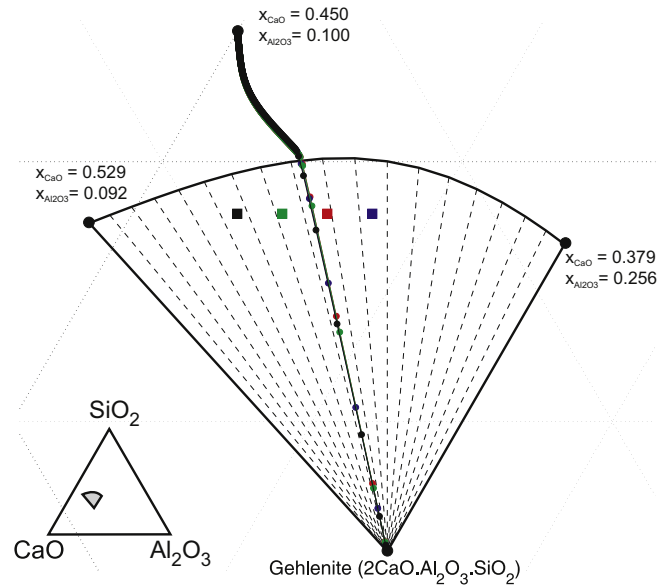

Fig. 5. Magnification of the isothermal section at 1400 °C at the two-phase gehlenite-liquid region to investigate the influence of the artificial Gibbs energy of the stoichiometric phase, gehlenite. The four squares indicate which tie-lines were considered to construct the paraboloid Gibbs energy. From the resulting coinciding diffusion profiles, it is clear that this artificial Gibbs energy has minimal influence on the results.

the whole composition domain. To avoid numerical problems with solving the system of Eqs. (8) and (9) in the first time steps, the paraboloid is constructed so that the stoichiometric phase is initially in equilibrium with the liquid phase. In a ternary system, the liquid interface composition is a priori not known. Fig. 5 shows, however, that this initial equilibrium, used to construct the paraboloid, does not affect steady-state growth of the solid phase. The four squares in Fig. 5 indicate the total system compositions used to define the initial equilibrium or tie-line. Since the resulting tie-lines from the four simulations coincide, it is clear that the constructed paraboloid Gibbs energy will have a minimal influence on the results if the paraboloids are taken to be at least 10 times steeper than the Gibbs energies of the solution phase.

5.3. Wollastonite crystallizing in a CaO–Al₂O₃–SiO₂ melt

A second simulation is done with the system composition in the two-phase region wollastonite-liquid at 1350 °C, for which the isothermal section is given in Fig. 3. Wollastonite (CaO·SiO₂) is located at the boundary of the composition domain (edge of phase diagram) and therefore its Gibbs paraboloid is moved slightly inwards and constructed with a stoichiometric composition at $(x^0_{CaO} = 0.499, x^0_{Al_2O_3} = 0.002)$. As the initial condition, a nucleus of 12 grid points of wollastonite is placed at the left side of the simulation domain. The initial liquid concentra-

tion is $(x^0_{CaO} = 0.455, x^0_{Al_2O_3} = 0.06)$, while the solid is initialized at its stoichiometric composition. The resulting composition profiles for steady-state growth are plotted in Fig. 6 and mapped on a ternary diagram in Fig. 7. Fig. 7 shows that the tie-line, going through the initial liquid composition, is not selected due to uphill diffusion of CaO during growth of wollastonite. The diffusion profile of CaO in Fig. 6 goes through a minimum because of two competing effects. Close to the solid–liquid interface, CaO diffuses uphill because of the steep gradient in Al₂O₃ concentration. Further away from the interface, the gradient in Al₂O₃ becomes smaller and CaO diffuses according to its own concentration gradient.

5.4. Tie-line selection in a ternary system

The influence of the diffusion mobilities on the tie-line selection is clearly shown in Figs. 4 and 7. In a diffusion-controlled phase transformation $L \rightarrow S$ in a ternary system, the interface velocity v is determined by two simultaneous flux balances at the interface:

$$\frac{1}{V_m}(x_{CaO,L} - x_{CaO,S})v = J_{CaO,L} - J_{CaO,S} \quad (30)$$

$$\frac{1}{V_m}(x_{Al_2O_3,L} - x_{Al_2O_3,S})v = J_{Al_2O_3,L} - J_{Al_2O_3,S} \quad (31)$$

where the growth of a shape-preserving (planar, cylindrical, spherical) solid is parabolic in time, $s = \alpha\sqrt{t}$ [19]. The growth rate constant α and the resulting tie-line, or interface concentration $x_{k,i}$, can be found by solving these flux balances simultaneously. For the crystallizing wollastonite,
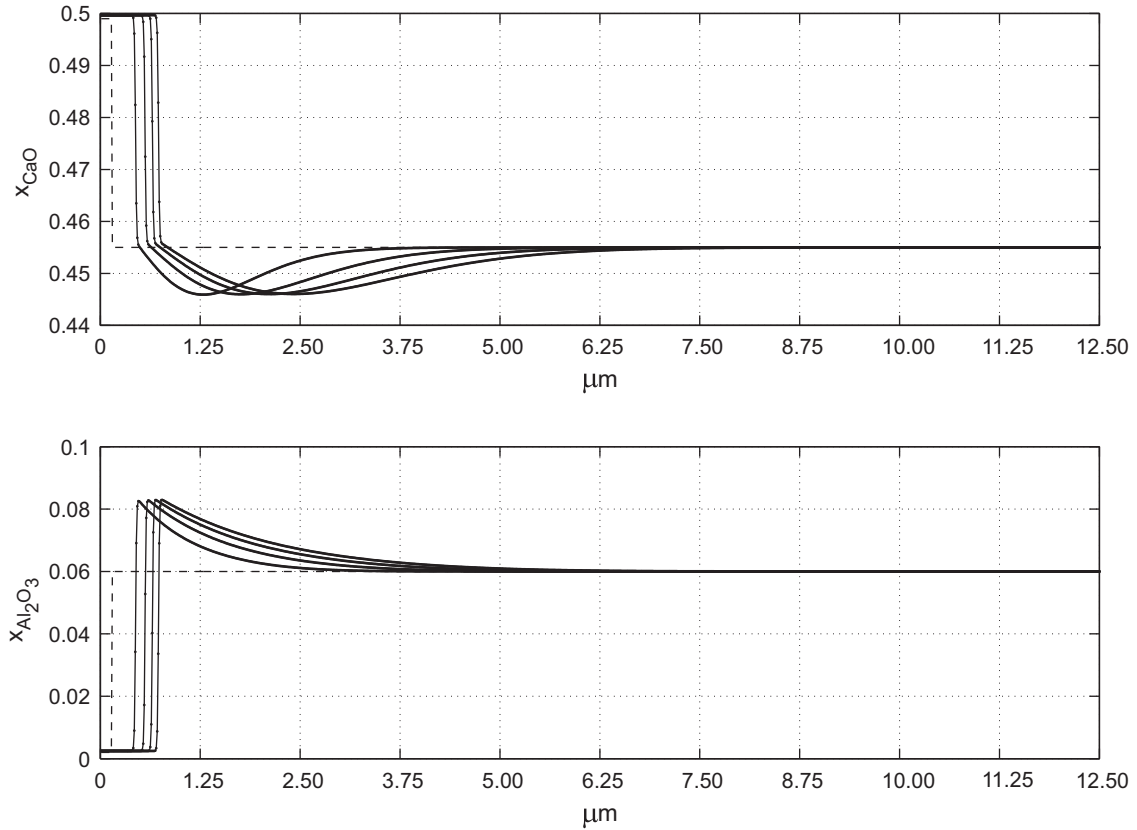
Fig. 6. Diffusion profiles of CaO and Al$_2$O$_3$ after a phase field simulation of crystallizing wollastonite in CaO–Al$_2$O$_3$–SiO$_2$ at 1350 °C. The profiles of x_{CaO} show a clear uphill diffusion effect. The interface composition of the liquid is at the solid–liquid phase boundary, as shown in Fig. 7. The dashed line is the initial composition profile. The time between the plotted profiles is 7 ms and the total system length is 12.5 μm.

in Fig. 7, α was determined from the phase field simulation, giving $\alpha = 3.5 \times 10^{-6}$ m s$^{-1/2}$. An analytical solution for this problem is only available for constant diffusivities and if cross-diffusion effects are neglected or one species diffuses much faster than the other [32,33], neither of which is the case in the considered oxide systems. On the other hand, a phase field model incorporates the full diffusion matrix correctly for all phases and ensures chemical equilibrium at the interface if the interface mobility is chosen appropriately [16]. Therefore, it will automatically select the correct tie-line and interface velocity, obeying the equations above. Figs. 7 and 4 show the tie-line selection for crystallizing and dissolving phases in oxide melts and its dependency on the diffusion mobilities. A phase field model is thus an elegant tool with which to investigate crystallization in higher order systems and predict tie-line selection with arbitrary diffusion properties.

5.5. Dendritic crystallization of wollastonite

A number of 2-D simulations is done with a similar setup to that used in Section 5.3. In this series of simulations, the interfacial energy of the solid–liquid interface is varied from 0.3 to 0.6 J m^{-2} and the resulting interface morphologies are plotted in Fig. 8. The sixfold anisotropy was observed experimentally [34]. For a given under- or
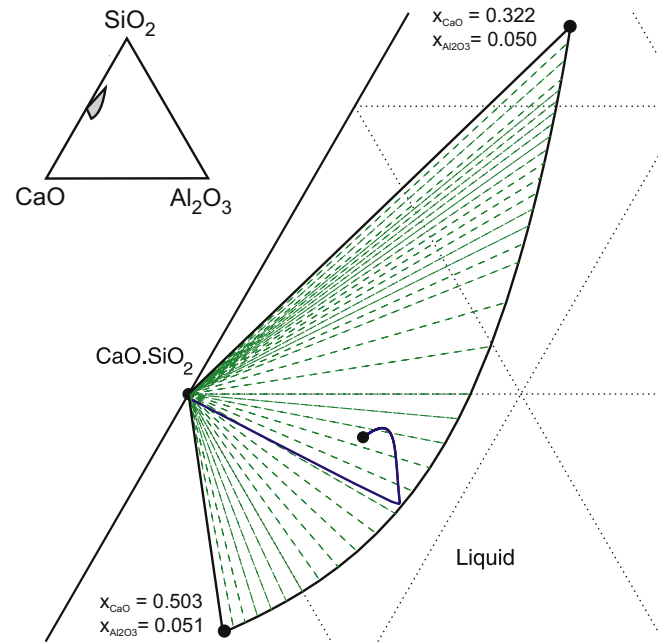

Fig. 7. Magnification of the isothermal section at 1350 °C at the two-phase wollastonite-liquid region. The simulation result of crystallizing wollastonite is plotted on this section. This figure shows that the tie-line with the initial liquid composition is not selected during growth of wollastonite under these conditions because of strong cross-diffusion interactions in the liquid. The dots indicate the initial composition of the solid and liquid phases.
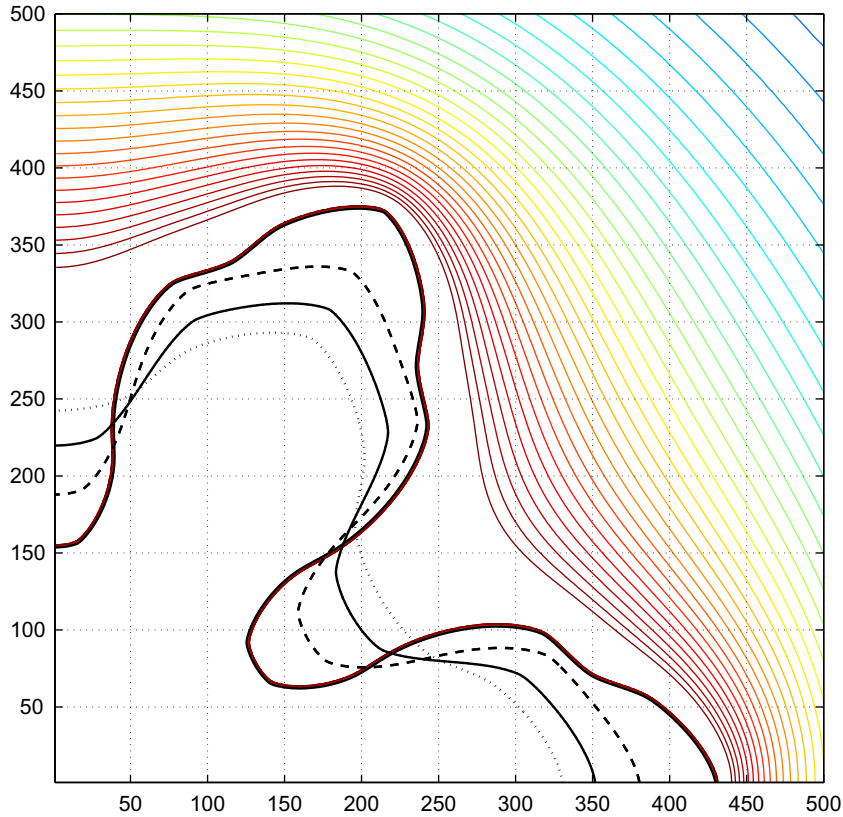
Fig. 8. Simulation results of 2-D crystallization of wollastonite in a CaO–Al$_2$O$_3$–SiO$_2$ melt with four different surface energies, 0.3 (outer solid), 0.4 (dashed), 0.5 (solid) and 0.6 J m^{-2} (dotted), and sixfold symmetry as observed in experiments. As the interfacial energy increases, the tip radius increases while the dendrite tip velocity decreases. For the simulation with $\sigma = 0.3$, the diffusion field of Al$_2$O$_3$ is plotted as well. The system size is 1000×1000, which equals 12.5×12.5 μm, and the total simulation time for all four cases was 0.2226 s. Only the left lower quarter of the simulation domain is plotted to increase the readability.

supersaturation Δ of the melt, the Peclet number $p = \frac{\rho v}{2-D}$ is determined by the Ivantsov formula [35]:

$$\Delta = \sqrt{\pi p} \ \exp(p)\mathrm{erfc}(\sqrt{p}) \tag{32}$$

This solution for free-growing needle crystals without interfacial energy does not select separate values for the dendrite tip radius ρ or its velocity v. Only if interfacial energy is taken into account is a single set of (ρ, v) selected. Fig. 8 shows that, for increasing interfacial energy, the dendrite tip radius ρ increases while the velocity decreases. A more detailed study of the crystallization behavior of wollastonite and comparison with experiments will be elaborated in future work.

6. Conclusions

The presented phase field model is able to describe isothermal crystallization of stoichiometric solid phases in oxide melts. The interfacial mobility can show strong anisotropy and the interfacial energy can have weak anisotropy to treat both faceted and dendritic crystallization. The thermodynamic functions in the model are retrieved from the FACT database for oxide systems using ChemApp. The Gibbs energies of stoichiometric phases are con-

structed assuming a paraboloid composition dependence. It is shown that the construction of the paraboloid function has a negligible effect on the tie-line selection if the paraboloid is at least 10 times steeper than the Gibbs energies of the solution phases. Three case studies of crystallizing and dissolving phases in an oxide melt are discussed. It is illustrated that the model can treat arbitrary diffusion effects, such as uphill diffusion, that influence phase transformations in multi-component systems. Finally, in combination with experiments, the model will be very helpful to study the effect of interfacial energy and anisotropy on dendrite growth in ternary and multi-component oxide melts.

References

[1] Kirkpatrick RJ. Am Mineral 1975;60:798.
[2] Campforts M, Verscheure K, Boydens E, Van Rompaey T, Blanpain B, Wollants P. Metall Mater Trans B 2007;38:841.
[3] Durinck D, Jones PT, Blanpain B, Wollants P, Mertens G, Elsen J. J Am Ceram Soc 2007;90:1177.
[4] Orrling C, Sridhar S, Cramb AW. ISIJ Int 2000;40:877.
[5] McMillan PW. Glass-ceramics. Academic Press; 1979.
[6] Kingery WD. J Appl Phys 1959;30:301.
[7] Kurz W, Fisher DJ. Fundamentals of solidification. Enfield Publishing & Distribution Company; 1998.
[8] Moelans N, Blanpain B, Wollants P. CALPHAD 2008;32:268.
[9] Kobayashi R. Physica D 1993;63:410.
[10] Warren JA, Boettinger WJ. Acta Metall Mater 1995;43:689.
[11] Steinbach I, Pezzolla F, Nestler B, Seesselberg M, Prieler R, Schmitz GJ, et al. Physica D 1996;94:135.
[12] Tiaden J, Nestler B, Diepers HJ, Steinbach I. Physica D 1998;115:73.
[13] Pelton AD, Chartrand P. Metall Mater Trans A 2001;32:1355.
[14] Moelans N, Blanpain B, Wollants P. Phys Rev B 2008;79:024113.
[15] Kim SG, Kim WT, Suzuki T. Phys Rev 1999;60:7186.
[16] Moelans N. Acta Mater 2011;53:1077.
[17] Eiken J, Boettger B, Steinbach I. Phys Rev E 2006;73:066122.
[18] Eriksson G, Pelton AD. Metall Trans B 1993;24:807.
[19] Kirkaldy JS. Can J Phys 1958;36:907.
[20] Uehara T, Sekerka RF. J Cryst Growth 2003;254:251.
[21] Heulens J, Moelans N. Scripta Mater 2010;62:827.
[22] Oishi Y, Nanba M, Pask JA. J Am Ceram Soc 1982;65:247.
[23] Bale CW, Belisle E, Chartrand P, Decterov SA, Eriksson G, Hack K, et al. CALPHAD 2009;33:295.
[24] Eriksson G, Hack K, Petersen S. ChemApp – a programmable thermodynamic calculation interface. In: Hirsch J, editor. Werkstoff Woche '96, symposium 8, simulation, modellierung, informationssysteme. DGM Informationsgesellschaft Verlag; 1997. p. 47–51.
[25] Hu SY, Murray J, Weiland H, Liu ZK, Chen LQ. CALPHAD 2007;31:303.
[26] Press WH, Teukolsky SA, Vetterling WT, Flannery BP. Numerical recipes in FORTRAN 77: the art of scientific computing. Cambridge University Press; 1999.
[27] Vlaamse-Overheid. Vlaams supercomputer centrum, Departement Economie, Wetenschap en Innovatie; 2010.
[28] Karma A, Rappel W-J. Phys Rev E 1996;53:R3017.
[29] Courtial P, Dingwell DB. Geochim Cosmochim Acta 1995;59:3685.
[30] Sugawara H, Nagata K, Goto KS. Metall Mater Trans B 1977;8B:605 [We have discovered that the diffusion coefficients in the abstract of this reference are erroneous. The values in the diffusion matrix of equation (27) are therefore too large. However, the approach and conclusions, presented in this work, are not affected. An erratum on Ref. [30] is being published soon.].
[31] Kim SK. Acta Mater 2007;55:4391.
[32] Coates DE. Metall Mater Trans 1972;3:1203.
[33] Coates DE. Metall Mater Trans 1972;4:1077.
[34] Heulens J, Guo X, Blanpain B, Moelans N. Unpublished work; 2010.
[35] Ivantsov GP. Dokl Akad Naut SSR 1947;58:567.